

## **Modelling Mesh Independent Transverse Cracks in Laminated Composites with a Simplified Cohesive Segment Method**

**Luiz F. Kawashita<sup>1</sup>, Alexandre Bedos<sup>2</sup> and Stephen R. Hallett<sup>3</sup>**

**Abstract:** A methodology is proposed for modelling transverse matrix cracks in laminated composites in a three-dimensional explicit finite element analysis framework. The method is based on the introduction of extra degrees of freedom to represent the displacement discontinuity and the use of a cohesive zone model to determine damage evolution and crack propagation. The model is designed for the analysis of matrix cracks in laminates made of uni-directional fibre-reinforced plies, allowing several assumptions to be made which greatly simplify the algorithm. This was implemented in the commercial software Abaqus/Explicit as a user-defined element subroutine (VUEL). The methodology was verified via the analysis of open-hole tension tests considering both  $\pm 45^\circ$  and quasi-isotropic layups. The results were found to be in qualitative agreement with experimental observations in terms of the nucleation and propagation of matrix cracks, the progressive delamination behaviour and the evident interactions between these damage mechanisms.

**Keywords:** composites, explicit, cohesive, mesh independent, fracture, delamination

### **1 Introduction**

Carbon-fibre reinforced composites manufactured from uni-directional plies are becoming the material of choice for large structural components in aerospace applications. The failure of these materials under quasi-static or impact overloading is highly complex and usually involves a combination of three damage mechanisms, namely delamination, transverse cracking and fibre failure [Green et al. (2007),

<sup>1</sup> School of Engineering, Cardiff University, Cardiff CF24 3AA, Wales, UK. Email: KawashitaL@cardiff.ac.uk

<sup>2</sup> Eole Nationale Supérieure des Mines de Saint-Etienne, F-42023 Saint Etienne, France.

<sup>3</sup> Advanced Composites Centre for Innovation and Science (ACCIS), University of Bristol, Bristol BS8 1TR, UK.

Hallett et al (2009)]. In order to achieve optimal designs in terms of weight reduction, damage tolerance and extended service life the progressive damage behaviour of the material must be predicted with accuracy. The interactions between the different damage mechanisms can be very complex and difficult to model using analytical or numerical methods. For this reason much of the design of high-performance composite structures still relies on large amounts of experimental testing which are both costly and time-consuming.

In many cases an accurate analysis of the progressive failure of composites requires the use of fracture mechanics considerations. The ability to model fracture processes within the finite element analysis framework has improved considerably after the introduction of robust numerical tools such as the virtual crack closure technique (VCCT) [Rybicki and Kanninen (1977)] and cohesive zone models (CZM) implemented in the form of interface elements [e.g. Alfano and Crisfield (2001), Camanho et al. (2003), Yang and Cox (2005), Pinho et al. (2006), Jiang et al. (2007)]. However, a major drawback of these methods is that they require *a priori* knowledge of the possible paths of each crack. This is not a significant problem for delamination which always occurs along well defined inter-ply interfaces; however it is difficult to pre-determine the locations of intra-ply transverse matrix cracks. Including these cracks in the finite element mesh additionally makes it extremely complex and too costly for practical industrial use. It has however been shown that interaction between matrix cracks and delamination has a critical part to play in determining the overall failure process [Green et al. (2007), Hallett et al. (2009)].

It is possible to model cracks and other discontinuities independently of the mesh definition via the introduction of enrichment functions in the finite element approximation. The extended finite element method (XFEM) [Belytschko and Black (1999)], which makes use of the partition of unity property of finite element shape functions [Melenk and Babuska (1996)], has been studied extensively in the past decade for various problems involving static or moving discontinuities [Fries and Belytschko (2010)]. Several variants and further developments have also been proposed, and of particular relevance are the consideration of cohesive cracks [Wells and Sluys (2001), Møes and Belytschko (2002)], the description of the discontinuity using phantom nodes [Hansbo and Hansbo (2004), Song et al. (2006), van der Meer and Sluys (2009)], the analysis of multiple overlapping cohesive segments [Remmers et al. (2003)] and the analysis of dynamic crack growth [Menouillard et al. (2006), Song et al. (2008), Nistor et al. (2008), Remmers et al. (2008)]. Although a number of codes have been developed for academic purposes, commercial implementations of XFEM are still in their infancy and may lack the robustness to solve problems involving multiple cracks in complex structures.

The aim of the present work was to develop and implement a simple and effec-

tive algorithm for the analysis of mesh-independent transverse cracks in laminated composites. This was intended to be a high-fidelity modelling tool for ply-level models solved using explicit time-integration schemes. The use of explicit finite element analysis has been found to be greatly beneficial in overcoming convergence difficulties of implicit analyses in the case of highly non-linear and unstable composites failure, even when loading is quasi-static [Jiang et al. (2007), Hallett et al. (2009), Kawashita and Hallett (2012)]. Particular emphasis was placed on numerical robustness so that the technique could be applied in the analysis of realistic composite structures typical of aerospace applications. The formulation presented here was specifically designed to model laminates made from unidirectional plies. Therefore several assumptions could be made which greatly simplified its implementation, enabling its introduction in the commercial finite element software Abaqus/Explicit by means of a user-defined element subroutine.

The model presented here is the result of an effort to develop a practical method for modelling transverse cohesive cracks in ply-level meshes using explicit finite element software. The main aim was to replace the use of pre-defined crack paths adopted in previous work [e.g. Jiang et al. (2007), Hallett et al (2009)] with mesh-independent cohesive cracks that followed a similar set of assumptions.

It should be noted that there is a large body of literature on the analysis of strong discontinuities and discrete cohesive cracks in finite element models. Relevant papers include Song et al. (2006), van der Meer and Sluys (2009), Armero and Linder (2009) among others. The model proposed here presents however a combination of features that results in great simplicity in terms of its implementation, which translates into numerical robustness and the ability to analyse large realistic problems. These features include (i) a series of simplifying assumptions suitable for the analysis of laminates, (ii) the use of an explicit solver, and (iii) the compatibility of the code with user-defined element subroutines found in commercial finite element software.

The next section describes in detail the characteristics of the algorithm and the main assumptions made. In Section 3 test cases are analysed which demonstrate the ability of the model to predict the initiation and propagation of multiple matrix cracks.

## 2 Model formulation

### 2.1 Element formulation

The baseline formulation for ‘undamaged’ elements is the 8-node fully-integrated linear isoparametric hexahedral element. Once a discontinuity is introduced, the domain is sub-divided using linear pentahedral elements as will be discussed later.

A linear-elastic orthotropic constitutive law is used to model the fibre-reinforced plies. However, in order to allow future developments of the code (e.g. the implementation of continuum damage models and rate-dependent material behaviour), the constitutive law has been written in terms of an objective stress rate, which also makes the user-defined elements consistent with the elements provided in Abaqus/Explicit. The stress rate is based on the rate-of-deformation tensor  $\mathbf{D}$  and the spin tensor  $\mathbf{W}$ ,

$$\mathbf{D} = \frac{1}{2} (\mathbf{L}^T + \mathbf{L}), \text{ and } \mathbf{W} = \frac{1}{2} (\mathbf{L} - \mathbf{L}^T), \quad (1)$$

where  $\mathbf{L}$  is the velocity gradient. The constitutive law is then written in rate form based on the Jaumann stress rate given by,

$$\dot{\boldsymbol{\sigma}} = \mathbf{C} : \mathbf{D} + \mathbf{W} \cdot \boldsymbol{\sigma} + \boldsymbol{\sigma} \cdot \mathbf{W}^T, \quad (2)$$

where  $\mathbf{C}$  is the material stiffness matrix. When evaluating the constitutive equation, a full Gauss quadrature is used as depicted in Figure 1a (which shows a planar representation of the 3D elements).

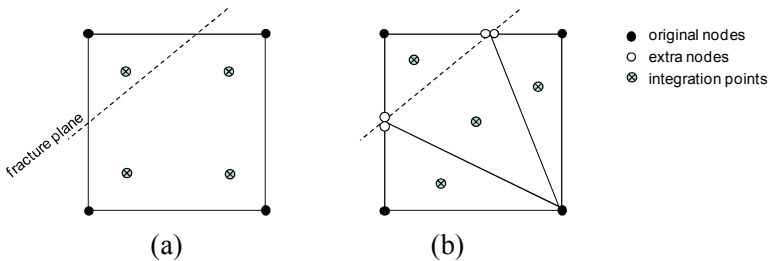


Figure 1: Planar representation of a fully-integrated 3D hexahedral element (a) which is split into pentahedral sub-domains with the introduction of extra nodes (b).

## 2.2 Displacement discontinuity and extra nodes

When the element is ‘damaged’ a strong discontinuity is introduced so that two independent displacement fields exist. To resolve the displacement jump between these fields, eight ‘extra’ nodes are introduced as shown in Figure 1b. These nodes are initialised as four coincident pairs so that the initial displacement jump across the discontinuity is zero. Their initial displacements and velocities are obtained by linear interpolation of nodal values from the original hexahedral element. For

example, the velocities of a new node located at the parametric coordinates  $\xi$  are initialised by,

$$\mathbf{v}(\xi) = \sum_{n=1}^8 N_n(\xi) \mathbf{v}_n, \quad (3)$$

where  $N_n$  are the standard shape functions of the original isoparametric element and  $\mathbf{v}_n$  are the velocities at the original nodes. Because the extra nodes are initially positioned along an edge of the original element, equation (3) simplifies to a linear interpolation between two nodes only.

In order to consider the two displacement fields independently a change is required from the original integration scheme. The hexahedral element is therefore ‘triangulated’ into multiple pentahedral sub-domains with two integration points each (which appear as one in the top view of Figure 1b). Stresses and other state variables are projected onto the new integration points using the same standard shape functions  $N_n$ . This requires the use of modified parametric coordinates  $\tilde{\xi}$  in the range  $\tilde{\xi}_i \in [-\sqrt{3}, \sqrt{3}]$  so that the coordinates of the original Gauss points  $\xi_i = \pm 1/\sqrt{3}$  become  $\tilde{\xi}_i = \pm 1$ . For example, the stresses at a new integration point with coordinates  $\tilde{\xi}$  are given by,

$$\boldsymbol{\sigma}(\tilde{\xi}) = \sum_{n=1}^8 N_n(\tilde{\xi}) \boldsymbol{\sigma}_n, \quad (4)$$

where  $\boldsymbol{\sigma}_n$  are the stresses at the original Gauss points.

Once the element has been divided into sub-domains and the new nodes and integration points have been initialised, the element operations (interpolation of field variables, evaluation of the constitutive equation and integration of internal forces) are then performed for every sub-domain independently using the appropriate shape functions for the linear pentahedral element.

The code is structured to cope with changes in the interpolation and integration schemes with minimal disruption to the solution. This is also facilitated by the ‘element-by-element’ nature of the explicit solution algorithm which does not require the assembly of global matrices. At the start of the simulation enough memory is allocated for each element taking into account the maximum number of integration points and extra nodes that could be required upon fracturing. The element computations are coded in a way that allows for simple looping over multiple sub-domains of either hexahedral or pentahedral formulation. Although the initialisation of new nodes and integration points require a number of additional operations, they are performed only once when an element fractures. After that, two pentahedral sub-domains will have roughly the same computational cost of one hexahedral

element for interpolation and integration. However further computational costs will incur with the introduction of a cohesive segment as described next.

### 2.3 Cohesive law

Damage evolution and crack propagation are determined using a cohesive zone modelling (CZM) approach. This method avoids the need for treating singular or oscillatory stress fields that appear in linear elastic analyses because the gradual softening behaviour of the interface ensures finite tractions within the cohesive zone. It is also a proven modelling tool for analysing composites delamination and fracture [Petrossian and Wisnom (1998), Alfano and Crisfield (2001), Camanho et al. (2003), Yang and Cox (2005)] and is particularly robust when using explicit time-integration [Pinho et al. (2006), Jiang et al. (2007)]. The main disadvantage of CZM is the requirement for good resolution of the cohesive zone ahead of the crack tip, which means that relatively fine meshes are usually needed for accuracy [Turon et al. (2007), Harper and Hallett (2008)].

The eight extra nodes added to each fractured element form a quadrilateral cohesive segment where the displacement jump is interpolated linearly. Here a single cohesive integration point is used for simplicity, as this has been shown to be accurate in practical applications [Hallett et al. (2009)]. The mixed-mode formulation presented by Jiang et al. (2007) is employed, and the reader should refer to that article for further details about the model. Traction-separation laws of linear softening are assumed as shown in Figure 2a. The subscripts I and II refer to mode-I (opening) and resultant mode-II (shear) respectively, while the subscript  $m$  denotes an arbitrary mode-mixity. The superscripts  $e$  and  $f$  refer to the critical separations at the elastic limit and failure, respectively.

To initiate fracture a quadratic criterion is used, i.e.

$$\sqrt{\left(\frac{\langle\sigma_{22}\rangle}{\sigma_I^{\max}}\right)^2 + \left(\frac{\sqrt{(\sigma_{12})^2 + (\sigma_{23})^2}}{\sigma_H^{\max}}\right)^2} = 1, \quad (5)$$

where the numerical indices follow the usual notation for composite materials (1 for the fibre direction and 3 for the out-of-plane direction),  $\sigma_I^{\max}$  and  $\sigma_H^{\max}$  are the cohesive strengths in mode-I and mode-II, respectively, and  $\langle\bullet\rangle$  denotes the McCauley operator. It should be noted that equation (5) is based on the assumption that the transverse crack is orthogonal to the plane 1-2 of the material. In reality, the presence of transverse shear stresses  $\sigma_{23}$  may cause the transverse crack to initiate at a different angle with respect to the plane 1-2. This could require lower resultant shear stresses for crack initiation, however it would also produce larger crack areas

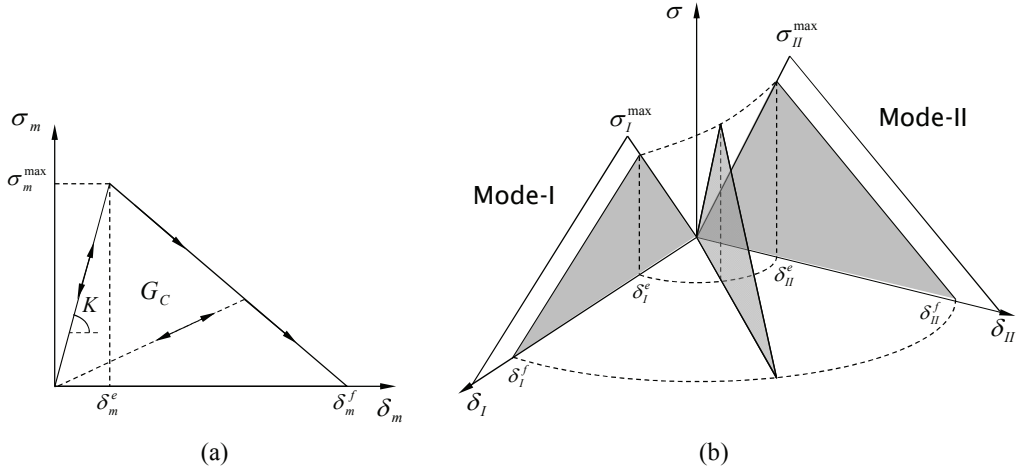


Figure 2: (a) mixed-mode bilinear traction-separation law and (b) decomposition into mode-I (opening) and mode-II (shear) components

which would dissipate more cohesive energy. Therefore equation (5) is thought to offer a good approximation especially for laminates containing large numbers of thin plies.

For damage propagation a power-law interaction is assumed between the strain energy release rates (SERR) in modes I and II,

$$\left(\frac{G_I}{G_{IC}}\right)^n + \left(\frac{G_{II}}{G_{IIC}}\right)^n = 1, \quad (6)$$

where  $G_{IC}$  and  $G_{IIC}$  are the critical SERR for pure modes I and II respectively. The power-law coefficient  $n$  is found by fitting experimental data from mixed-mode tests. This coefficient was set to 1 in this work, which gives a good fit for the material under consideration [Jiang et al. (2007)]; therefore equation (6) will retrieve a linear interaction criterion.

The graphical interpretation of the adopted mixed-mode formulation is shown in Figure 2b. The ratio between modes I and II is estimated at every time step based on the current ratio between the displacement jump components. Again following the usual notation for composite materials we have,

$$\delta_I = \langle \delta_{22} \rangle \text{ and } \delta_{II} = \sqrt{(\delta_{12})^2 + (\delta_{23})^2}. \quad (7)$$

Overclosure of the crack surfaces is minimised with the enforcement of a constant penalty stiffness of magnitude  $K_I$  which opposes the interpenetration of the surfaces when  $\delta_I$  is negative. Frictionless contact is assumed throughout.

When a cohesive segment is introduced in a pristine element, the initial displacement jump must be zero while the initial cohesive tractions must match the local stress state. Therefore, the use of a cohesive law of finite stiffness requires the traction-separation curve, Figure 2a, to be ‘shifted’ to the left so that the maximum traction occurs at zero separation [van der Meer et al. (2012)]. This shifted displacement jump is defined as,

$$\tilde{\delta} = \delta - \delta_e, \quad (8)$$

which applies to both modes of loading (I and II).

Equation (8) shows that if the stresses in the vicinity of an active cohesive segment are relaxed the interface will acquire a residual displacement jump of  $-\delta_e$ . This means that a small permanent deformation is introduced locally whenever a new a cohesive segment is initialised, with its magnitude being inversely proportional to the assumed cohesive stiffness. Although this residual deformation is unwanted, its effects will be minor and only observable if active cohesive segments are unloaded prior to failure. Therefore this effect will be negligible when compared for example with the global stiffness change that is introduced when potential cracks are meshed using cohesive elements.

## 2.4 Time-integration scheme

The extra nodes introduced when an element splits are not accessible to the Abaqus/Explicit solver and therefore must be managed and updated inside the user sub-routine. Following the assembly of the internal force vector, the extra nodes are updated via a modified central difference rule. At a given time increment  $k$ , the half-step velocities are obtained via,

$$\mathbf{u}_{k+1/2} = \mathbf{u}_{k-1/2} + \frac{\Delta t_{k-1/2} + \Delta t_{k-1/2}}{2} (\mathbf{M}^{-1} \mathbf{f}^{int}), \quad (9)$$

where  $\mathbf{M}$  is the diagonal mass matrix,  $\Delta t$  is the time step size and  $\mathbf{f}^{int}$  is the internal force vector. The nodal displacements for the increment  $k+1$  are then given by,

$$\mathbf{u}_{k+1} = \mathbf{u}_k + \Delta t_{k+1/2} \dot{\mathbf{u}}_{k+1/2}. \quad (10)$$

The splitting of elements and the introduction of cohesive segments may generate local stress imbalances that can result in high-frequency ‘noise’ in the dynamic solution. Depending on the amplitude of these oscillations and the size of the newly

created sub-domains numerical instabilities can arise. Therefore an optional viscous damping term  $c$  is defined so that the velocity update for extra nodes becomes,

$$\dot{\mathbf{u}}_{k+1/2} = \dot{\mathbf{u}}_{k-1/2} + \frac{\Delta t_{k-1/2} + \Delta t_{k+1/2}}{2} [\mathbf{M}^{-1} (\mathbf{f}^{int} - c \dot{\mathbf{u}}_{k+1/2})]. \quad (11)$$

It should be noted that viscous damping will reduce the stable time increment and may generate spurious forces under rigid body motion, so this parameter should be used with caution. In the present work, and when necessary, appropriate values for  $c$  were determined ‘empirically’ by performing series of simulations, starting with  $c=0$  and increasing this value until the numerical instability was overcome.

All the results presented in this paper have been analysed using a range of values for the mass scaling and viscous damping parameters to verify the sensitivity of the results to these values. It has been observed that the peak loads and patterns of matrix cracks and delaminations are relatively insensitive to these parameters as long as the dynamic effects are negligible, as measured e.g. by the ratio between the amplitudes of the introduced vibrations with respect to the monotonic (‘quasi-static’) deformations, and the ratio between the kinetic and internal energies. This has confirmed previous observations using pre-defined crack paths, e.g. in Jiang et al. (2007) and Hallett et al. (2009).

## 2.5 Orientation and continuity of crack paths

When modelling fracture in isotropic materials, the direction of crack propagation is unknown and will depend on the stress state near the crack tip. However for matrix cracks in unidirectional composite plies the crack will always propagate parallel to the fibre direction, since the strength of the material along this plane is much lower than across the fibres. Therefore in the proposed model the in-plane direction of crack propagation is determined directly from the local fibre orientation. Moreover, along the thickness direction the crack will follow the 3-direction of the element coordinate system, so it will always be orthogonal to the ply surface as shown in Figure 3. As pointed out by van der Meer et al. (2012) the assumption of orthogonal through-thickness cracks is valid for in-plane tensile loading. However under compression the fracture planes will usually be ‘slanted’ at a certain angles which will depend upon the local stress state at the time of initiation [Puck and Schurmann (2002), Dávila et al. (2005)]. Since the analysis of in-plane compression is beyond the scope of the present work, such capability has not been required here.

Because the extra nodes are not ‘visible’ to the Abaqus/Explicit solver, no data related to them is written to the standard output database. Therefore algorithms had to be introduced in the user-defined subroutine to perform the writing of custom

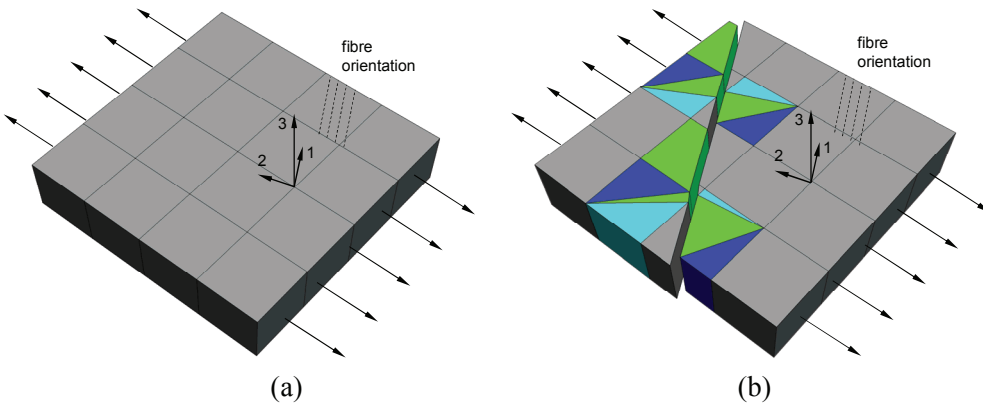


Figure 3: Crack propagation in a  $60^\circ$  off-axis tensile test, (a) original mesh and (b) after the nucleation and propagation of a solution-dependent crack

data files at regular time intervals. These files contained various types of data including the coordinates of original and extra nodes, stress and strain components, state variables etc. Generic visualisation software could then be used to access, visualise and manipulate these data.

Because a CZM approach is used, no singularities will exist at the ‘numerical’ crack tip (i.e. the tip of the cohesive zone); however the mesh must be fine enough to provide a good resolution of the cohesive tractions [Harper and Hallett (2008)]. So in contrast to linear-elastic analyses, no special treatment is required for the crack tip element. Therefore the model could be further simplified via two assumptions, namely (i) the crack propagates in a stepwise fashion, fully traversing elements at once, and (ii) the displacement jump vanishes at the element edge where the numerical crack tip lies. These assumptions are not uncommon in the analysis of cohesive cracks [e.g. Remmers et al. (2003) and van der Meer and Sluys (2009)].

Figure 4 illustrates the crack propagation behaviour. If no cracks exist in the vicinity of the element when the initiation criterion is met [equation (7)], the crack will pass through the critical integration point as shown in Figure 4a. Once introduced, the cohesive segment will cross the entire element, but the displacement jump will be zero before the crack propagates. On the other hand, if a crack already exists in the vicinity of the element, the situation depicted in Figure 4b takes place. In this case the continuity of the path is enforced independently of the location of the critical integration point. Neighbouring elements will then ‘share’ the extra nodes activated along the common edge, while the newly created nodes will remain constrained until the crack propagates further.

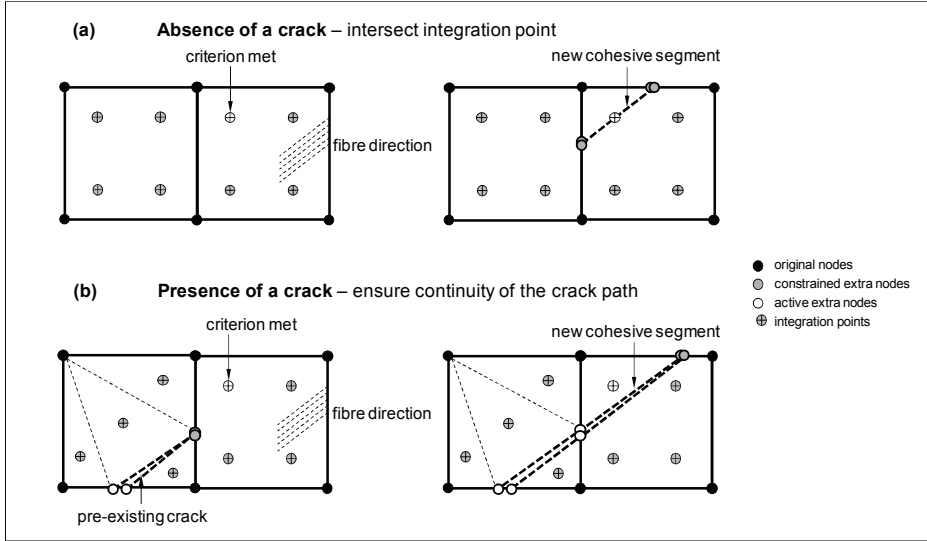


Figure 4: Introduction of a new cohesive segment within the element

## 2.6 Time-step considerations

Explicit schemes such as the central difference method utilised here are only conditionally stable, requiring the time increment size to be below a critical maximum to ensure numerical stability. This critical time increment is given by the Courant criterion,

$$\Delta t_{crit} = \frac{l_e}{w}, \quad (12)$$

where  $w$  is the speed of sound in the material and  $l_e$  is the smallest equivalent element length in the direction of wave propagation. Because the ply thickness is constant, the element lengths in the 3-direction will usually be constant (in ply-level models). Moreover, if the mesh is of good quality then the in-plane aspect ratio of the elements will be close to 1. Following these assumptions, equation (12) may be approximated as,

$$\Delta \bar{t}_{crit} = \sqrt{A \frac{\rho}{E_{11}}}, \quad (13)$$

where  $\rho$  is the material density,  $E_{11}$  is the elastic modulus in the fibre direction, and  $A$  is the in-plane area of the smallest integration sub-domain in the model. Equation (13) shows that as the integration volume approaches zero the critical

stable increment vanishes. Therefore in order to avoid extremely small time steps (and consequently extremely expensive solutions) some level of control is required over the sub-domain size. In the proposed model this control is achieved via the definition of a single scalar safety factor  $\alpha$ , so that the minimum sub-domain length is set to be  $L \alpha$ , where  $L$  is the characteristic length of the original (parent) element. This concept is illustrated in Figure 5, again using a planar representation of 3D elements. In this example, because the mesh is structured and the element size is constant, the length  $L \alpha$  can be seen as a critical radius surrounding every node. If the predicted path of a propagating crack (dashed line) intersects an element edge at a distance smaller than  $L \alpha/2$ , two options exist. If the distance is greater than or equal  $L \alpha/2$ , the intersection point is moved away from the node to enforce a minimum sub-domain size, as shown by the solid line in Figure 5a (an example of this can be seen in Figure 3b). However, if the distance is smaller than  $L \alpha/2$ , the crack is set to pass exactly through that node, Figure 5b. It should be noted that many other patterns of crack propagation deriving from these assumptions are also taken into account, including cracks running along element boundaries, elements being split exactly into two pentahedrals, etc.

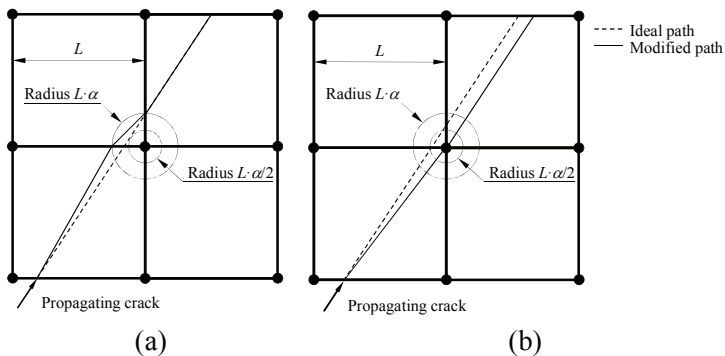


Figure 5: Changes to the crack path for time-step considerations; (a) enforcing a minimum sub-domain size or (b) intersecting a node.

In the present work the value of  $\alpha = 0.1$  has been assumed throughout. Figure 6 shows an example of crack propagation in an unstructured mesh using this value. It can be seen that the effective crack paths are not perfectly straight lines, however the effects of such small deviations are thought to be negligible. Additionally, deviations are minimised as the mesh is further refined.

For  $\alpha = 0.1$ , the value of  $A$  for the smallest sub-domain in Figure 5a is 200 times lower than that for the original element. Therefore in this case the stable time increment  $\Delta\bar{t}_{crit}$  would drop by a factor  $\sqrt{200}$  upon crack propagation, which would

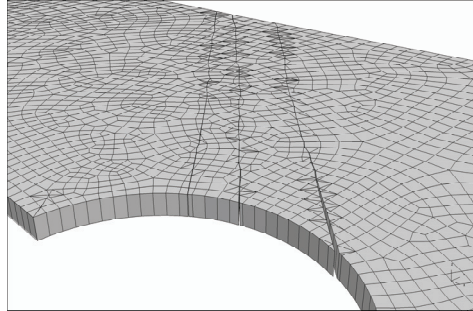


Figure 6: Crack propagation in an unstructured mesh showing small deviations from ideal straight lines

mean a larger than 14-fold increase in run time. For the simulation of quasi-static loading, one alternative is to use a selective mass-scaling procedure. This is done by scaling the material density  $\rho$  for every sub-domain individually so that their stable increments  $\Delta\bar{t}_{crit}$  remain the same as for the original element. The total mass of the fractured element will then be the mass of the original element multiplied by the number of sub-domains generated (one, two or four depending on the splitting pattern). However, the percentage mass increase in the model will often be negligible since elements are usually small, and this effect will also be minimised with further mesh refinement.

## 2.7 Crack density control

Because the elements can be intersected by one discontinuity only, crack branching and intersection are not allowed. If two parallel cracks attempt to traverse the same element then one will arrest permanently at the element edge. Therefore an artificial control over the maximum density of cracks must be introduced. This type of control is often used when modelling crack initiation in solids using mesh-independent methods [e.g. Iarve (2003), van der Meer and Sluys (2009)].

In the present work the crack density is indirectly controlled via the definition of a critical radius from the ‘numerical’ crack tip (i.e. the beginning of the cohesive zone) within which no further crack initiation is allowed to occur. The procedure is illustrated in Figure 7. The initiation is suppressed for all elements whose centroids lie within the radius  $R_{min}$  from an active numerical crack tip (shaded elements Figure 7), except for the element directly adjacent to it.

As this procedure is meant to avoid unwanted crack ‘intersections’, the definition of an appropriate radius  $R_{min}$  will depend on the size of the largest elements in the mesh,  $L_{max}$ . Therefore the theoretical lower bound for the critical radius should be

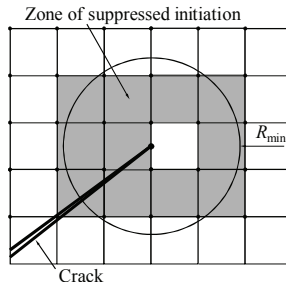


Figure 7: Illustration of the crack density control algorithm. Initiation is suppressed within a radius  $R_{\min}$  from the beginning of the cohesive zone, except for the element directly adjacent to it

$R_{\min} > L_{\max}$  (although as will be shown in later sections a safety margin should be applied to this value). On the other hand the radius  $R_{\min}$  should be as small as possible to minimise its interference on the analysis and allow true solution-dependent crack initiation. For the notched tensile tests analysed here the range of values under consideration was  $L_{\max} < R_{\min} < 2L_{\max}$ .

### 3 Analysis of open-hole tension tests

Prior to the analysis of more complex cases, the model presented here has been verified extensively using simpler meshes subjected to various load configurations. The results have been compared with those obtained with the use of pre-defined crack paths in Abaqus/Explicit using the continuum hexahedral elements type C3D8 and the cohesive elements type COH3D8. Virtually identical results have been obtained in terms of strains and stress distributions and global force-displacement behaviour when the same mesh, boundary conditions and material properties were used (the model proposed here outputs the location of the cracks in the undeformed configuration, which then facilitates the construction of the equivalent model using pre-defined crack paths for comparison). However, in order to investigate the ability to reproduce the interactions between delaminations and matrix cracks, open-hole specimens have been analysed and we focus on these results in this paper.

Open-hole tension tests are practical and effective methods to evaluate the progressive damage behaviour of laminates [Green et al. (2007), Hallett et al. (2009)]. These tests have the major advantage of generating a controlled stress concentration around the open hole which promotes the initiation and propagation of the various damage modes in a reproducible manner. The small specimen geometry proposed by Green et al. (2007) was considered here with a width of 15.875 mm, a hole

diameter of 3.175 mm and a gauge length of 63.5 mm (of which only the central 31.75 mm are modelled in the finite element analysis). The material investigated in this work is the Hexcel® IM7/8552 pre-preg system, and its basic mechanical properties have been provided by Jiang et al. (2007) and are summarised in Tables 1 and 2. The cohesive stiffnesses  $K_I$  and  $K_{II}$  in Table 2 were estimated from the isotropic mechanical properties of the resin system, i.e. a Young's modulus  $E = 4.67$  GPa and Poisson's ratio  $\nu = 0.33$ , assuming that the interfacial stiffness represents the elastic deformation of a resin-rich layer of 0.01 mm in thickness [Kawashita and Hallett (2012)]. Two different layups were considered as described next.

Table 1: Elastic properties for unidirectional IM7/8552 laminates

$E_{11}$ [GPa]	$E_{22}$ [GPa]	$E_{33}$ [GPa]	$\nu_{12}$	$\nu_{13}$	$\nu_{23}$	$G_{12}$ [GPa]	$G_{13}$ [GPa]	$G_{23}$ [GPa]
161.0	11.38	11.38	0.32	0.32	0.436	5.17	5.17	3.962

Table 2: Cohesive properties for unidirectional IM7/8552 laminates

$G_{IC}$ [N/mm]	$G_{IIC}$ [N/mm]	$\sigma_I^{\max}$ [MPa]	$\sigma_{II}^{\max}$ [MPa]	$K_I$ [N/mm $^3$ ]	$K_{II}$ [N/mm $^3$ ]
0.2	1.0	60	90	$4.67 \times 10^5$	$1.75 \times 10^5$

### 3.1 $\pm 45^\circ$ layup, $[+45_2/-45_2]_S$

Open-hole tension tests using a symmetric  $[+45_2/-45_2]_S$  layup have been proposed recently as a benchmark for validating and comparing XFEM codes [Oguntoye and Hallett (2011)]. The specimen dimensions and the adopted finite element mesh are shown in Figure 8. The cured ply thickness was 0.125 mm. Only a half-model was required due to the through-thickness symmetry. Each ply block (containing two plies) was meshed with one element through the thickness and modelled using the proposed user-defined elements. The interface between the ply blocks was modelled using the cohesive elements COH3D8 provided by Abaqus/Explicit. A rather coarse mesh was used in this study with element sizes varying gradually from 0.125 mm around the open-hole to 0.5 mm at the extremities. This resulted in 14,696 continuum elements, 7,348 cohesive elements and 30,032 nodes for the half-model. In order to analyse quasi-static loading with acceptable run times, a global mass-scaling procedure was used with a density scale factor of  $10^5$ , resulting in a stable time increment of approximately  $2 \times 10^{-6}$  s (which includes appropriate

safety factors). In order to reduce the computational cost associated with the analysis of these quasi-static tests with a serial explicit dynamic code, the thermal residual stresses have been neglected. This resulted in considerably shorter run times as this avoided the initial ‘thermal’ step in the calculation. Loading was introduced via the application of smoothly-varying displacement boundary conditions to both ends of the model. The crack density control parameter was  $R_{\min} = 1$  mm and a viscous coefficient  $c = 10^{-4}$  kg s<sup>-1</sup> was assumed. Simulations were run up to complete specimen separation, which was achieved after approximately 160,000 time increments and an extension of 0.51 mm. A typical double-precision job running on a single CPU clocked at 3 GHz took approximately 11 h to complete. In its current version, the code cannot run in ‘parallel’ execution mode using multiple CPUs. Considerable reductions in run-time could be achieved with the parallelisation and optimisation of the code, and this is the focus of ongoing work.

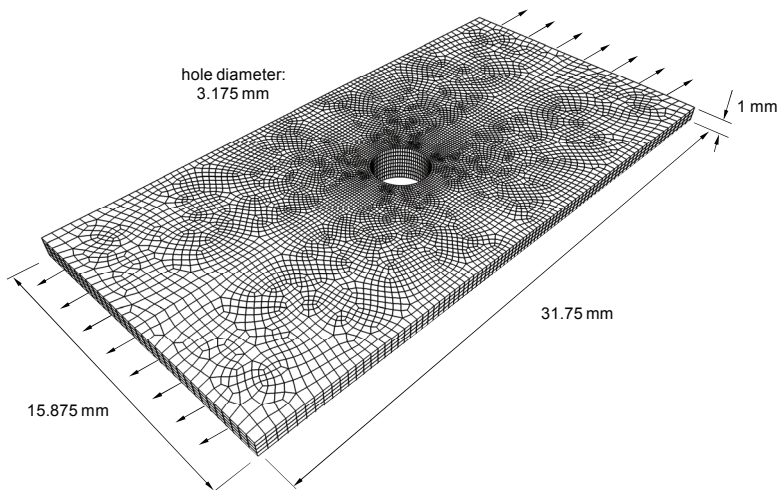


Figure 8: FE mesh for the open-hole tension specimen, layup  $[+45_2/-45_2]s$

Figure 9 shows a typical deformed mesh after failure. The overall pattern is very similar to that observed experimentally by Oguntoye and Hallett (2011), with matrix cracks running from the sides of the open-hole towards the edges of the specimen, combined with widespread delamination allowing complete specimen separation. Results are presented in terms of the applied ‘far-field’ stress which is defined as the total applied load divided by the gross cross-sectional area. Figure 10 shows the resulting stress-extension data for this test. Also shown for comparison are the average experimental failure stress and the numerical results presented by Oguntoye and Hallett (2011). The latter were obtained using the XFEM capability

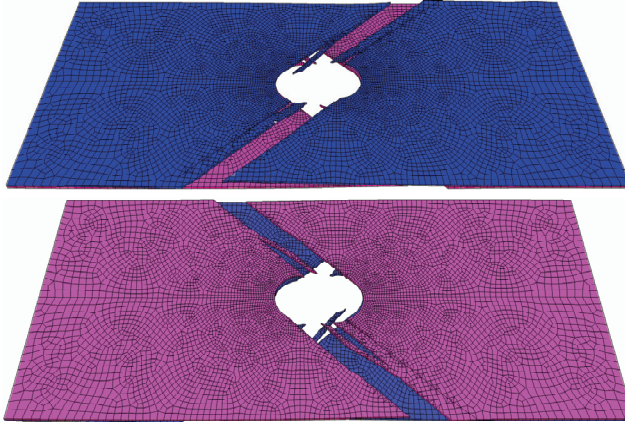


Figure 9: Pattern of matrix cracks after complete separation for the open-hole tension specimen, layup  $[+45_2/-45_2]_S$  (top and bottom views of a half-model through the thickness)

provided by Abaqus/Standard assuming the same set of material properties shown in Tables 1 and 2 and using two levels of mesh refinement (it should be noted that the XFEM tool in Abaqus/Standard is in fact a phantom node/CZM formulation) [Dassault Systèmes (2010)].

It can be seen that the numerical failure stress obtained with the proposed model is approximately 30% higher than the experimental average value; however it is very close to the XFEM predictions, especially those with a coarse mesh. The main reasons for the differences observed with respect to the experimental failure stress are believed to be (i) the absence of flaws in the numerical model as opposed to real specimens, which might contain imperfections especially after the drilling process; (ii) the assumption of linear elastic in-plane shear behaviour; and (iii) the absence of thermal residual stresses in the model.

The differences between the proposed model and the XFEM analyses are attributed to different reasons. Firstly, the use of explicit time integration, mass-scaling and a viscous damping parameter are likely to have contributed to an artificially higher failure stress (although the XFEM formulation also makes use of a viscous regularisation scheme). Secondly, the XFEM capability only accounts for the propagation of one crack at a time within the enrichment domain [Dassault Systèmes (2010)], while a larger number of cracks is considered in the present work.

The interactions between matrix cracks and delaminations predicted with the proposed model are illustrated in Figure 11, where maps of activated cohesive seg-

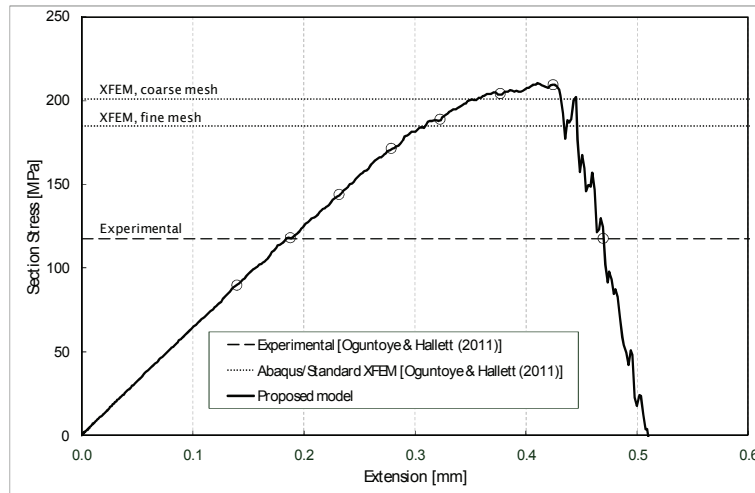


Figure 10: Stress-extension data for the open-hole tension specimen, layup  $[+45_2/-45_2]_S$  (symbols mark the times shown in Figure 11)

ments are superimposed to the contours of delamination damage at different points in time. It should be noted that the crack patterns in Figure 11 represent all initialised cohesive segments including those with nonzero cohesive tractions. It can be seen that the delamination pattern is clearly influenced by the location of matrix cracks. Delaminations initiated near the open hole and propagated towards the edge of the specimen following the paths of propagating matrix cracks. The major load drop in Figure 10 is associated with delamination propagation across the whole specimen width. A sharp load drop would be expected at this point; however the mass-scaling procedure combined with the use of a viscous damping parameter resulted in a more gradual load drop.

### 3.2 Quasi-isotropic (QI) layup, $[+45_2/90_2/-45_2/0_2]_S$

The second test case is the open-hole tension specimen with a ply-level scaled quasi-isotropic (QI) layup, i.e.  $[45_2/90_2/-45_2/0_2]_S$  [Green et al. (2007)]. The finite element meshes and model assumptions in this case were very similar to those used in the previous example. However the model was nearly twice as large with 4 ply blocks and 3 interfaces (for the half-model) with a total of 29,391 continuum elements, 22,044 cohesive elements and 60,064 nodes. In this case a job with the same number of time increments (160,000) took approximately 22 h to complete (again neglecting thermal residual stresses).

In order to investigate the influence of the crack density parameter, two different

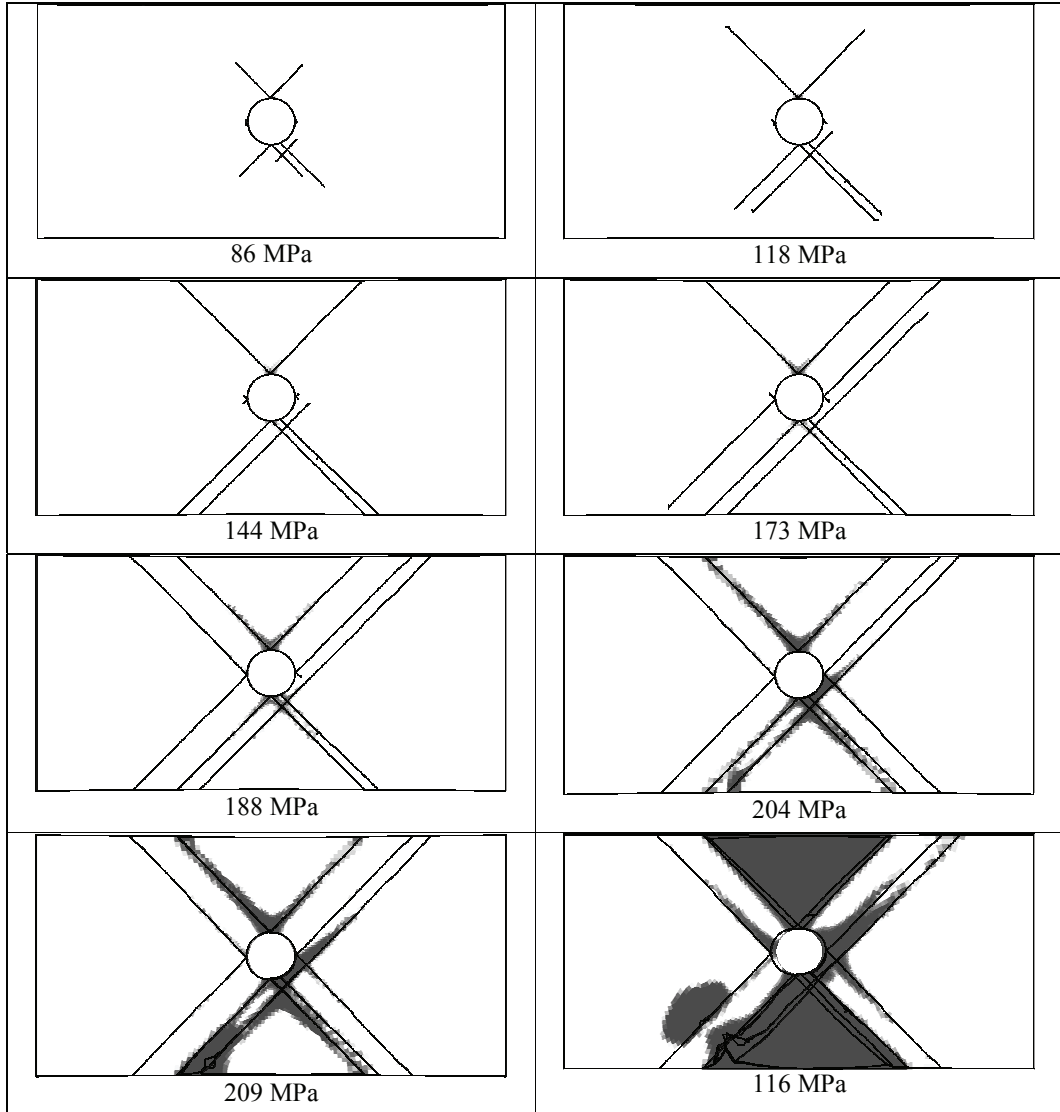


Figure 11: Interaction between matrix cracks and delamination for the open-hole tension specimen with layup  $[+45_2/-45_2]_S$

values for  $R_{\min}$  were considered, namely 1.0 mm and 0.5 mm. ‘Failure’ of the specimen was defined as the point in time where delaminations propagated across the full width. Typical patterns of matrix cracks at failure are shown in Figure 12. Again it should be noted that all activated cohesive segments are displayed and not only fully failed segments. The patterns were similar for both cases, although a larger number of cracks was observed for the smaller value of  $R_{\min}$ .

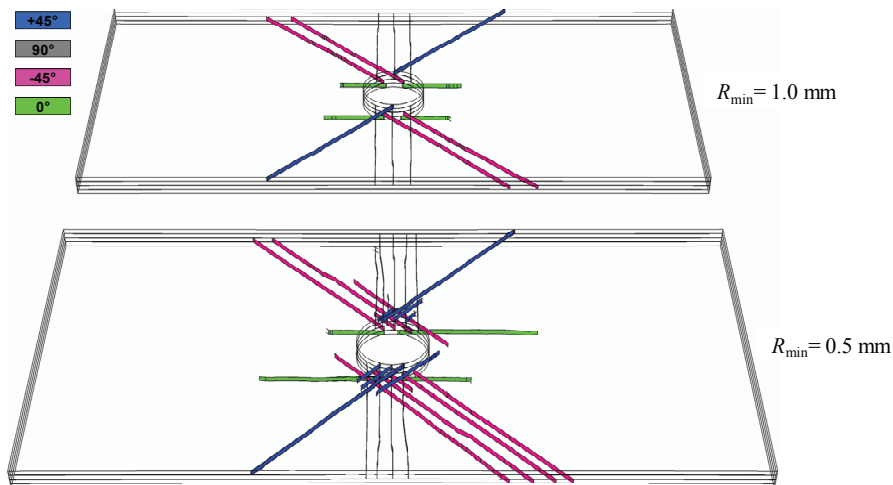


Figure 12: Typical patterns of matrix cracks for the open-hole tension specimen with QI layup  $[45_2/90_2/-45_2/0_2]_S$  (half-model through the thickness)

The resulting stress-extension curves are shown in Figure 13, where the average experimental failure stress reported by Green et al. (2007) is also plotted for comparison. It can be seen that the use of  $R_{\min}=0.5$  mm resulted in oscillatory behaviour and numerical instability prior to final failure. This was caused by spurious crack arrests due to the excessive proximity between neighbouring cracks. Although 0.5 mm is the exact maximum element length in the adopted mesh, it was not an appropriate choice for the radius  $R_{\min}$  because the algorithm enforces a minimum distance between active crack tips and not between cracks. This shows that a safety margin should be applied when determining appropriate values of  $R_{\min}$  for a given mesh size.

The analyses with  $R_{\min}=1.0$  mm on the other hand did not suffer from oscillations or instability. Nevertheless, similarly to what was observed for the  $\pm 45^\circ$  layup the numerical failure stresses were considerably higher than the experimental value. Possible reasons for the discrepancy are identified as the likely presence of defects in real specimens, the disregard of thermal residual stresses and the absence of

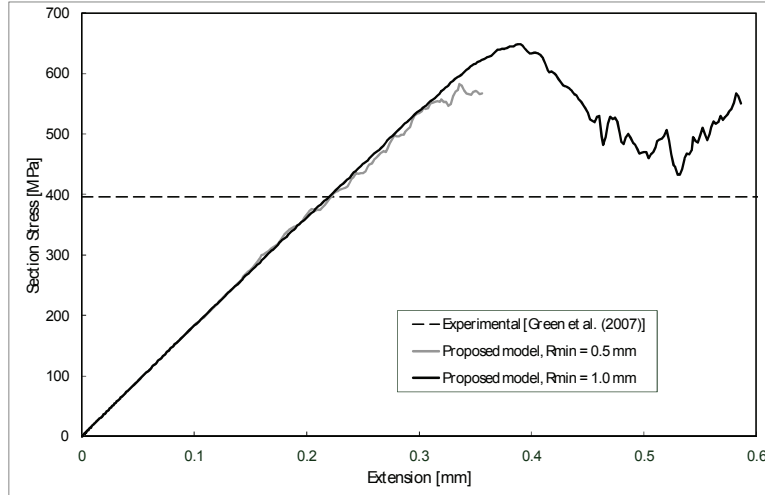


Figure 13: Stress-extension curves for the open-hole tension specimen of quasi-isotropic layup,  $[45_2/90_2/-45_2/0_2]_S$ .

damage model that accounts for local fibre breakage. The absence of a sharp load drop upon failure also suggests that the combination of mass-scaling and viscous damping may have contributed to a higher predicted failure stress as discussed earlier. However due of the presence of  $0^\circ$  plies (and the absence of a model for fibre failure) the applied load was not expected to return to zero after complete delamination.

The delamination and transverse cracking behaviour for both values of  $R_{\min}$  was similar, with the case  $R_{\min} = 0.5$  showing more damage for similar levels of applied stress. This is illustrated in Figure 14 where delamination damage and matrix cracking are compared for the same applied load (which corresponds to 85% of the failure load for  $R_{\min} = 1.0$  mm).

Delaminations and matrix cracks initiated near the edge of the hole at relatively low loads. Upon further loading, interface damage was observed also near the outer edges of the specimen especially along the  $+45^\circ/90^\circ$  ply interface. Interactions between matrix cracks and delaminations are evident throughout the damage process. Matrix cracks extending along the full width were first observed in the surface plies ( $+45^\circ$ ). This promoted the ‘joining-up’ of the delaminations propagating from the open-hole and the specimen edge along the  $+45^\circ/90^\circ$  ply interface, which was then followed by the catastrophic failure of the specimen.

Good qualitative agreement was observed between these results and the experi-

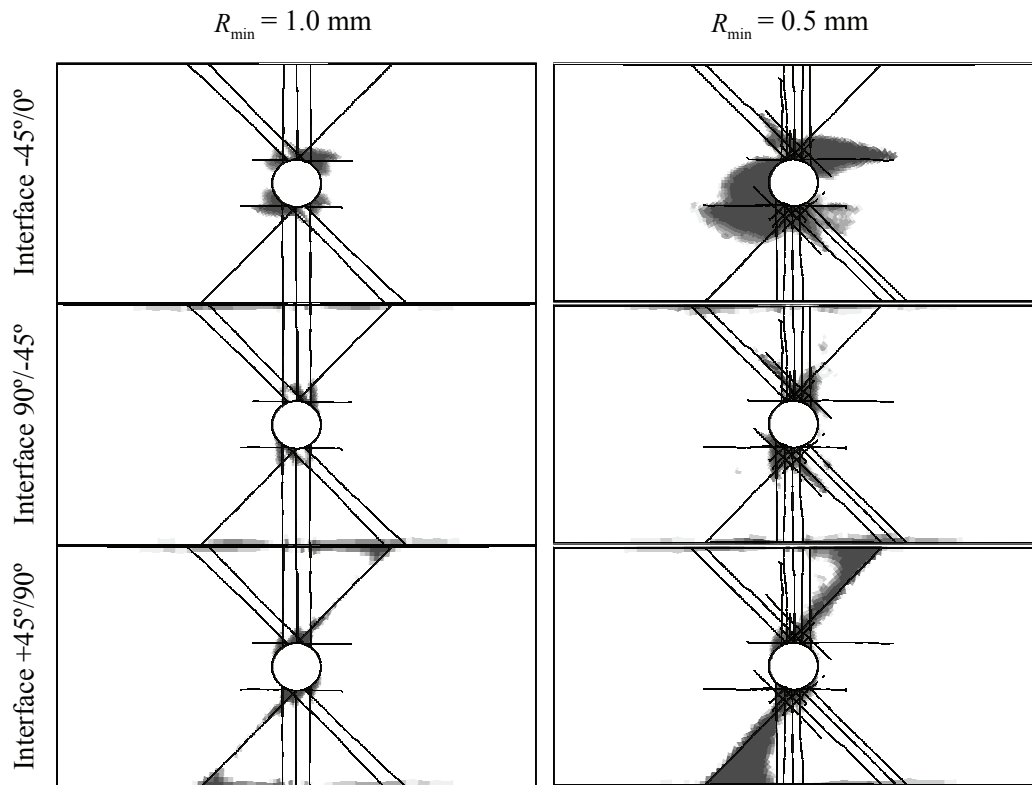


Figure 14: Delamination damage in the open-hole specimen (ply-level scaled quasi-isotropic layup) at 85% of the numerical failure load

mental and numerical observations reported by Hallett et al. (2009). However their predicted failure stress using pre-defined cohesive cracks was considerably lower at 434 MPa. This could be in part due to the different hole geometries as well as the assumed number and location of matrix cracks. However the coarser meshes used in the present work and the introduction of viscous damping in the formulation of matrix cracks are thought to be major factors contributing to the higher failure stresses observed here.

The use of standard cohesive elements to model delamination is another possible source of errors. This is because the cohesive element will remain connected to the original nodes even if these are on different sides of a discontinuity. In other words, the displacements will continue to be interpolated linearly within the cohesive element even after discontinuities have been introduced across the surface.

However, because each cohesive element usually covers a small surface area, these effects will be small and will also be minimised with further mesh refinement. One solution to this problem would be to evaluate the cohesive law directly at nodes instead of using interpolation via cohesive elements, as discussed in van der Meer et al. (2012). Although such a ‘discrete’ cohesive element is not readily available in Abaqus/Explicit, it could be implemented in the form of a user-defined nonlinear ‘spring’ element as described by Jiang et al. (2007). This is left as a recommendation for future work.

#### 4 Conclusions

A method has been proposed for the introduction of mesh-independent transverse cracks in finite element models analysed using explicit time-integration. The method supports the initiation and propagation of large numbers of solution-dependent cracks and uses a cohesive zone modelling approach to describe crack propagation. Because the formulation is designed for the analysis of matrix cracks in unidirectional composite plies, several assumptions could be made which simplified the formulation considerably. This enabled its implementation as a user-defined element subroutine in the commercial software Abaqus/Explicit. The model was verified via the analysis of open-hole tension tests with two different layups. Comparisons were made with experimental observations and numerical results available in the literature. Qualitative agreement was observed in terms of the nucleation and propagation of transverse cracks, predicted delamination patterns and the interactions between damage mechanisms. However the predicted failure stresses were considerably higher than those observed experimentally. Possible reasons include (i) the likely presence of defects in real specimens, (ii) the use of coarse meshes and (iii) the absence of thermal residual stresses in the analyses. The latter two are consequences of the long run-times observed for each analysis when using a serial version of the code. The parallelisation and optimisation of the code are the focus of ongoing work which aims at addressing these issues.

#### References

- Alfano, G.; Crisfield, M.A.** (2001): Finite element interface models for the delamination analysis of laminated composites: Mechanical and computational issues. *Int. J. Numer. Meth. Engng.*, vol. 50, pp. 1701-1736.
- Armero, F.; Linder, C.** (2009): Numerical simulation of dynamic fracture using finite elements with embedded discontinuities. *Int. J. Fract.*, vol. 160, pp. 119-141.
- Belytschko, T.; Black, T.** (1999): Elastic crack growth in finite elements with minimal remeshing; *Int. J. Numer. Meth. Engng.*, vol. 45, iss. 5, pp. 601-620.

**Camanho, P.P.; Dávila, C.G.; de Moura, M.F.** (2003): Numerical simulation of mixed-mode progressive delamination in composite materials. *J. Compos. Mater.*, vol. 37, pp. 1415-1438.

**Dassault Systèmes** (2010): Abaqus 6.10 Documentation.

**Dávila, C.G.; Camanho, P.P.; Rose, C.A.** (2005): Failure criteria for FRP laminates; *J. Compos. Mater.*, vol. 39, iss. 4, pp. 323–345.

**Green, B.G.; Wisnom, M.R.; Hallett S.R.** (2007): An experimental investigation into the tensile strength scaling of notched composites. *Compos. Part A-Appl. S.*, vol. 38, iss. 3, pp. 867-878.

**Hallett, S.R.; Jiang, W.G.; Khan, B.; Wisnom, M.R.** (2008): Modelling the interaction between matrix cracks and delamination damage in scaled quasi-isotropic specimens; *Compos. Sci. Tech.*, vol. 68, iss. 1, pp. 80-89.

**Hallett, S.R.; Green, B.G.; Jiang, W.G.; Wisnom, M.R.** (2009): An experimental and numerical investigation into the damage mechanisms in notched composites; *Compos. Part A-Appl. S.*, vol. 40, iss. 5, pp. 613-624.

**Hansbo, A.; Hansbo, P.** (2004): A finite element method for the simulation of strong and weak discontinuities in solid mechanics; *Comput. Method. Appl. M.*, vol. 193, pp. 3523-3540.

**Harper, P.W.; Hallett, S.R.** (2008): Cohesive zone length in numerical simulations of composite delamination. *Eng. Fract. Mech.*, vol. 75, iss. 16, pp. 4774-4792.

**Iarve, E.V.** (2003): Mesh independent modelling of cracks by using higher order shape functions; *Int. J. Numer. Meth. Engng.*, vol. 56, iss. 6, pp. 869–882.

**Jiang, W.G.; Hallett, S.R.; Green, B.G.; Wisnom, M.R.** (2007): A concise interface constitutive law for analysis of delamination and splitting in composite materials and its application to scaled notched tensile specimens. *Int. J. Numer. Meth. Engng.*, vol. 69, iss. 9, pp. 1982-1995.

**Kawashita, L.F.; Hallett, S.R.** (2012): A crack tip tracking algorithm for cohesive interface element analysis of fatigue delamination propagation in composite materials. *Int. J. Solids Struct.*, in press, DOI: 10.1016/j.ijsolstr.2012.03.034

**Li, X; Hallett, S.R.; Wisnom, M.R.** (2009): Numerical simulation of damage propagation in overheight compact tension tests. *17<sup>th</sup> International Conference on Composite Materials (ICCM 17)*, Edinburgh, UK.

**van der Meer, F.P.; Sluys, L.J.** (2009): A phantom node formulation with mixed mode cohesive law for splitting in laminates. *Int. J. Fracture*, vol. 158, iss. 2, pp. 107-124.

**van der Meer, F.P.; Sluys, L.J.; Hallett, S.R.; Wisnom, M.R.** (2012): Computational modeling of complex failure mechanisms in laminates; *J. Compos. Mater.*;

vol. 46, iss. 5, pp. 603-623.

**Melenk, J.M.; Babuska, I.** (1996): The partition of unity finite element method: Basic theory and applications; *Comput. Method. Appl. M.*, vol. 139, iss. 1-4, pp. 289-314.

**Menouillard, T.; Réthoré, J.; Combescure, A.; Bung, H.** (2006) Efficient explicit time stepping for the eXtended Finite Element Method (X-FEM). *Int. J. Numer. Meth. Engng.*, vol. 68, pp. 911-939.

**Möes, N.; Belytschko, T.** (2002): Extended finite element method for cohesive crack growth; *Eng. Fract. Mech.*, vol. 69, iss. 7, pp. 813-833.

**Nistor, I.; Pantale, O.; Caperaa, S.** (2008): Numerical implementation of the eXtended Finite Element Method for dynamic crack analysis; *Adv. Eng. Softw.*, vol. 39, iss. 7, pp. 573-587.

**Oguntoye, M.O.; Hallett, S.R.** (2011): A Benchmark Test for XFEM in Composites. *Dassault Systèmes UK Regional Users Meeting 2011*, 18th-20th October 2011, South Gloucestershire, UK.

**Pinho, S.T.; Iannucci, L.; Robinson, P.** (2006): Formulation and implementation of decohesion elements in an explicit finite element code. *Compos. Part A-Appl. S.*, vol. 37, iss. 5, pp. 778-89.

**Petrossian, Z.; Wisnom, M.R.** (1998): Prediction of delamination initiation and growth from discontinuous plies using interface elements. *Compos. Part A-Appl. S.*, vol. 29, pp. 503-515.

**Puck, A.; Schurmann, H.** (2002): Failure analysis of FRP laminates by means of physically based phenomenological models; *Compos. Sci. Tech.*, vol. 62, iss. 12-13, pp. 1633-1662.

**Remmers, J.J.C.; de Borst, R.; Needleman, A.** (2003): A cohesive segments method for the simulation of crack growth; *Comput. Mech.*, vol. 31, iss. 1-2, pp. 69-77.

**Remmers, J.J.C.; de Borst, R.; Needleman, A.** (2008): The simulation of dynamic crack propagation using the cohesive segments method; *J. Mech. Phys. Solids*, vol. 56, iss. 1, pp. 70-92.

**Rybricki, E.F.; Kanninen, M.F.** (1977): A finite element calculation of stress intensity factors by a modified crack closure integral; *Eng. Fract. Mech.*, 9, pp. 931-938.

**Song, J.H.; Areias, P.M.A.; Belytschko, T.** (2006): A method for dynamic crack and shear band propagation with phantom nodes; *Int. J. Numer. Meth. Engng.*; vol. 67, iss. 6, pp. 868-893.

**Song, J.H.; Wang, H.W.; Belytschko, T.** (2008): A comparative study on finite

element methods for dynamic fracture. *Comput. Mech.*, vol. 42, iss. 2, pp. 239-250.

**Turon, A.; Dávila, C.G.; Camanho, P.P.; Costa, J.** (2007): An engineering solution for mesh size effects in the simulation of delamination using cohesive zone models. *Eng. Fract. Mech.*, vol. 74, iss. 10, pp. 1665-1682.

**Wells, G.N.; Sluys, L.J.** (2001): A new method for modelling cohesive cracks using finite elements; *Int. J. Numer. Meth. Engng.*, vol. 50, iss. 12, pp. 2667-2682.

**Yang, Q.D.; Cox, B.** (2005): Cohesive models for damage evolution in laminated composites; *Int. J. Fracture*, vol. 133, iss. 2, pp. 107-137.